Nonlinear Dynamics 114(2): 110 (2026)
https://doi.org/10.1007/s11071-025-11867-w

Multistability in milling dynamics with tool runout

David Hajdu

Published: 20 January 2026

Abstract Traditional models used to study regenerative machine tool chatter often ignore the radial runout of multi-edge milling cutters and its influence on dynamic stability. This runout induces asymmetric forced vibrations within each spindle revolution, which can lead to irregular variations in the cutter-workpiece engagement and in the delay patterns of the cutting process. The actual dynamical system involves multiple time delays, fly-overs, and nonlinearities, which pose significant challenges for standard numerical solvers. In this study, a path-following continuation technique is employed to explore new periodic motions that emerge when runout is considered. The results reveal that the system's behavior is more complex than previously thought, with multiple stable and unstable solutions appearing within a specific range of technological parameters. Theoretical findings predicted by the improved model were successfully validated experimentally using a workpiece with a single dominant vibration mode. This work demonstrates the existence of isolated solution branches and bistability under realistic operating conditions.

Keywords Milling stability · Tool runout · Continuation · Time-delay · Bistability

David Hajdu
MTA-BME Lendület Machine Tool Vibration Research Group, Department of Applied Mechanics, Budapest University of Technology and Economics, Műegyetem rkp. 3., H-1111 Budapest, Hungary
Department of Applied Mechanics, Faculty of Mechanical Engineering, Budapest University of Technology and Economics, Műegyetem rkp. 3., H-1111 Budapest, Hungary
E-mail: hajdu@mm.bme.hu

1 Introduction

In the early 20th century, researchers observed that the machining quality strongly depends on the vibrations that arise during cutting processes [1]. The works of Tlusty and Spacek (1954) [2], as well as Tobias and Fishwick (1958) [3], identified the sources of undesired vibrations as a consequence of the loss of stability in the cutting operation. The *regenerative effect*—as it is termed—includes past motions of the tool and the workpiece, which are responsible for the unstable self-excited vibrations known as *chatter*. The corresponding mathematical equations are functional differential equations (FDEs) [4] that require deeper analysis than ordinary differential equations (ODEs). While in turning operations these models often reduce to autonomous delay-differential equations (DDEs), the problem is more complex in case of milling, where non-autonomous time-periodic delay-differential equations (TPDDEs) need to be studied.

The regenerative model paved the way for researchers to further investigate the dynamics of milling operations. Despite the complex nature of the problem, the earliest approaches in the literature were simple enough to treat the solution at (semi-) analytical level [5]. This led to the development of the so-called *stability lobe diagrams* (SLDs), which separate the domain of stable (chatter-free) and unstable machining parameters, typically, the spindle speed and dept of cut. These SLDs were intended to help machinists in the optimal design of cutting processes and to avoid the undesired vibrations. However, the reliability of the charts always depended on numerous factors, such as modeling and mathematical simplifications, as well as identification and measurement errors.

With the improvement of computational tools, numerical solvers enabled more accurate analysis of system dynamics. Among the widely used numerical approaches are the zero-order approximation [6], multi-frequency solution [7], collocation [8], semi-discretization [9], spectral element method [10], each offering distinct advantages for analysis. A more comprehensive review of numerical methods applied to the study of machine tool vibrations can be found in the work of Insperger et al. [11].

Although numerical algorithms have significantly evolved, most models used in the literature still rely on initial simplifications that may not hold under practical conditions. These reductions substantially reduce the reliability of classical prediction methods. Robust methods [12,13] and probabilistic approaches [14,15] were developed to address these challenges, but the real progress in machine tool research depends on a deeper understanding of the cutting mechanics itself. A chronological summary of uncertainty evaluation studies can be found in the work of Schmitz [16].

The importance of tool runout—often referred to as eccentricity—on the machining quality has been discussed in the works of Martellotti (1941) [17], Kline and DeVor (1983) [18], and Wang and Liang (1996) [19], among others. Their works present detailed studies on chip formation kinematics, chip load and surface quality, however, they did not investigate forced vibrations or dynamic stability. In the presence of runout, the geometric center point G of the tool is located on the axis of rotation A of the spindle, see Fig. 1. In order to characterize the imperfections generated by runout easily, a well-known model with two parameters is considered in the rest of this work [18]. These parameters are r and ψ, where r represents the absolute value of the runout (that is, the offset between the axis of rotation and the geometric axis of the tool), and ψ is an alignment angle that defines the position of the geometric axis relative to an arbitrarily selected tooth (e.g., tooth #1). The cutting edge points closer to A may not be engaged during the complete (revolution) period leaving more material to be removed by the subsequent flutes. Experiments also verified that tooth marks on the surface were distanced by the feed per revolution—the surface is mostly cut by the so-called "high tooth"—, instead of the typically expected feed per tooth [20]. This observation also indicates that the angles at which the subsequent teeth enter and exit can be different. Thus, the kinematic model also reveals that the cutter–workpiece engagement (CWE) is geometrically asymmetric for the neighboring cutting edges.

A common assumption in conventional milling models is that the CWE remains unaffected by the vibrations induced by periodic forcing. More precisely, the engagement of the cutting edge with the workpiece material is computed first (without vibrations), and no feedback mechanism is considered. It is like a rigid kinematic model, where the CWE is kept "frozen", even if it is not true. Nonetheless, this way of thinking is technically correct in case of ideal symmetric tools and cutting operations, where the ideal periodic motions indeed have no effect on the CWE. Similarly to linear systems, in this case we can first compute cutting forces, and solve the equation of motion, but its solution does not affect the force itself at all, and the equation is practi-

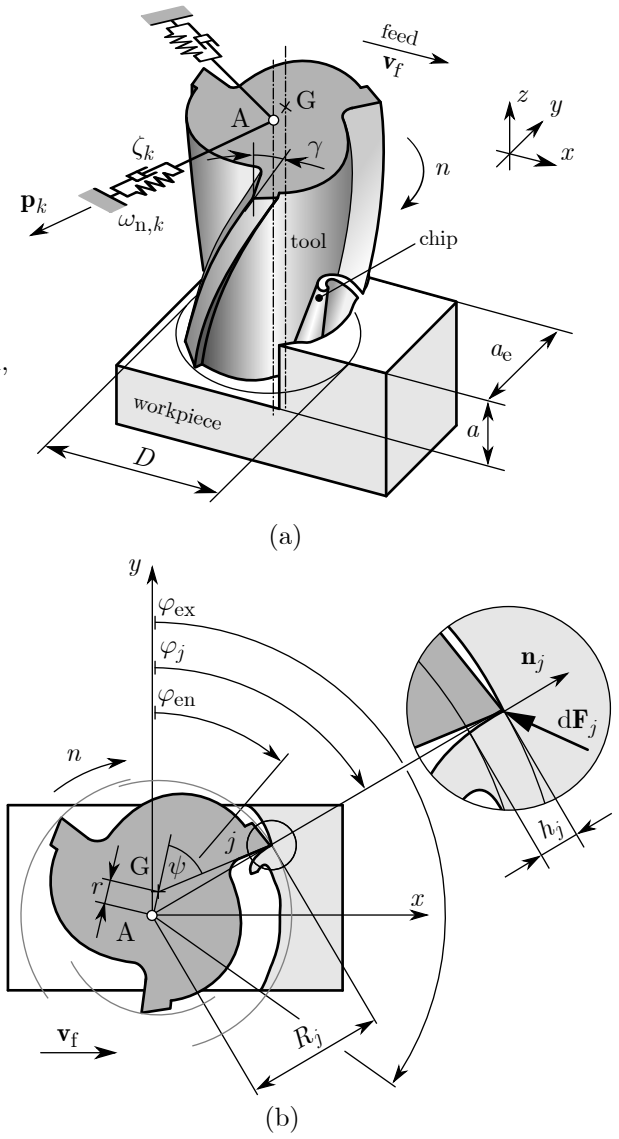

Fig. 1 Schematic figure of the dynamical model of milling (the runout is greatly enlarged). Due to tool misalignment, the axis of rotation A does not coincide with the geometric center G resulting in a radial runout caused by the offset between the two axes. (a) 3D-view on the dynamical model, (b) 2D-view on the cross-section highlighting the effect of runout.

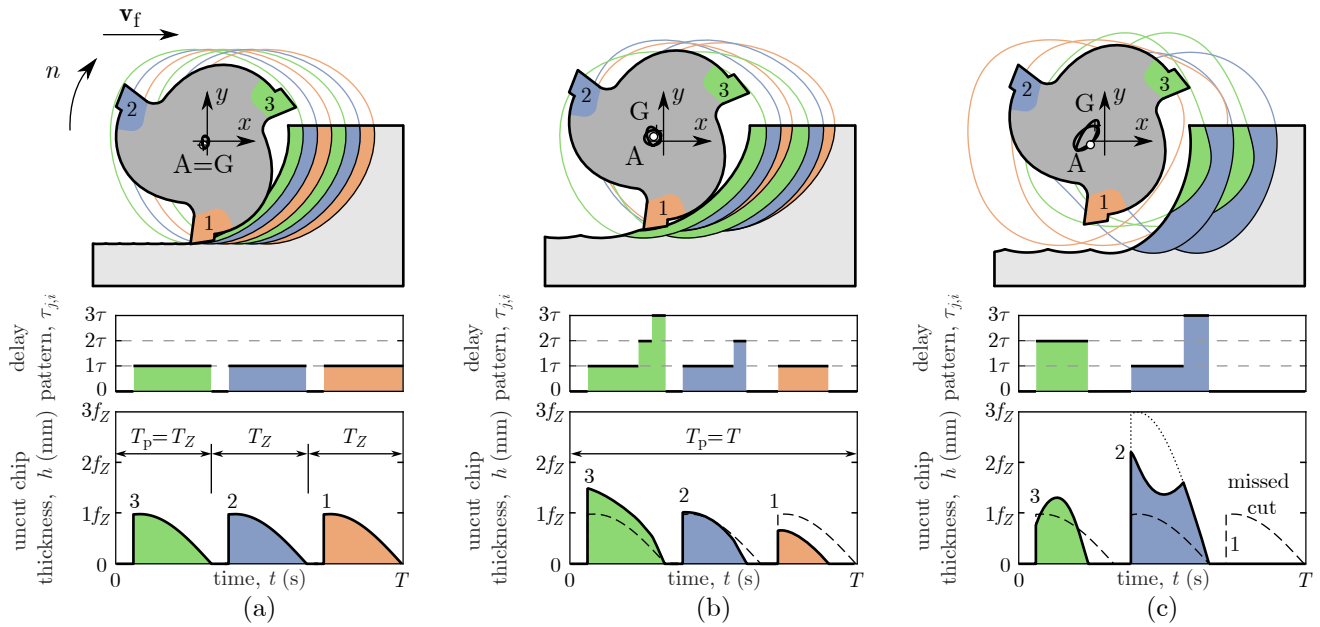

Fig. 2 Effect of runout on the cutter-workpiece engagement (the runout and vibrations are greatly enlarged for visualization purposes). (a) The exclusion of runout ($r = 0$ μm) results symmetric cutting periods for each tooth cycle, (b) minor tool runout changes the cutting cycles and the actual entering/exiting angles of the individual teeth, (c) elevated forced vibrations drastically change the cutter-workpiece engagement and the cutting cycles leading to highly altered delay patterns.

cally solved. Still, the cutting processes in milling are interrupted, inherently nonlinear and nonsmooth, and the equation of motion may not be solved in a linear manner. Specifically, in the presence of runout the forcing becomes dependent on the tool vibrations, and the two quantities cannot be separated as simply.

The frozen CWE can be used as an approximation—in spite of the mathematical incorrectness—if the effect of vibrations on the actual cutting edge engagements is minimal. Numerous studies utilized this approach [21,22,23,24,25,26], where the kinematic model included tool runout, however, the mathematical linearization was not performed around the true periodic motion. Only some time-domain simulations indicated that the conventional method may lack sufficient accuracy, as highlighted, for example, by Niu et al. [27].

Researchers eventually turned toward the nonlinear analysis of the dynamical model to achieve a more accurate representation of the physical process. The initial work of Faassen et al. [28] introduced an improved tool path model, though runout was not included in it; the nonlinearities in that study were originating from the trochoidal motion of the cutting edges. Later, in his thesis work [29], Faassen presented time-domain simulations and numerical bifurcation diagrams that revealed the effect of runout—referred to as eccentricity—, but experimental validation did not incorporate this effect. Bachrathy et al. [30] investigated a state-dependent delay model without considering runout and demonstrated that linear stability limits shift near resonances. More recently, Totis et al. [31] focused explicitly on runout, and showed that forced vibrations break the symmetry and alter the actual CWEs; see Fig. 2 and the detailed discussions later in Section 2. This phenomenon was further explored by Hajdu et al. [32], who experimentally observed and validated symmetry breaking effects across multiple scenarios.

The studies presented recently suggested that further elaboration is needed to enrich the understanding, as the numerical solvers were sometimes running into converge problems. The nature of the nonlinear dynamical equations implies that multiple solutions can coexist, however, these were not studied systematically before (not even in the works [31,32]). Such complexity of the solutions make the regular iterative approaches unreliable when the stability chart is scanned from point to point. Therefore, a pseudo-arclength numerical continuation technique was implemented in this work to clarify the topology of stability charts. The new theoretical findings were verified experimentally using a flexible workpiece with a single dominant vibration mode, but the predicted irregular vibrations can arise in general for multiple-degrees-of-freedom oscillatory systems, too. The topology insists that the complexity increases at lower spindle speed, and the stability charts can hide multiple (isolated) periodic motions.

The remainder of the paper is structured as follows. The dynamical model of milling, including tool runout,

is presented in Section 2. The discretization method and the computation of periodic solutions are also discussed in this section. Subsequently, an experimental case study is presented in detail in Section 3, which validates the importance of the correct numerical analysis and confirms the existence of multiple stable solutions. Finally, the results are summarized in Section 4.

2 Dynamical analysis of milling

2.1 Milling dynamics with tool runout

The standard multiple-degrees-of-freedom (MDoF) model of milling operations is presented in Fig. 1, where $\omega_{\mathrm{n},k}$ is the natural angular frequency ($k = 1, \dots, d$), ζ_k is the relative damping ratio, $\mathbf{U}_k$ is the mass-normalized mode shape vector, $\mathbf{p}_k$ is the corresponding geometrically normalized modal direction ($\mathbf{p}_k = \mathbf{U}_k/|\mathbf{U}_k|$), and d is the number of the modes. The equation of motion in this case can be written in the form

$$\ddot{\mathbf{q}}(t) + \hat{\mathbf{C}}\dot{\mathbf{q}}(t) + \hat{\mathbf{K}}\mathbf{q}(t) = \mathbf{U}^{\top}\mathbf{F}\left(t, \mathbf{r}_t\right), \tag{1}$$

where $\mathbf{q}(t) \in \mathbb{R}^d$ is the vector of modal coordinates, $\dot{\square}$ stands for differention w.r.t. time t, $\mathbf{U} = \mathrm{col}_{k=1}^{d}\mathbf{U}_k$ is the mass-normalized modal transformation matrix, while $\hat{\mathbf{C}} = \mathrm{diag}_{k=1}^{d}(2\zeta_k\omega_{\mathrm{n},k})$ and $\hat{\mathbf{K}} = \mathrm{diag}_{k=1}^{d}(\omega_{\mathrm{n},k}^2)$ are diagonal matrices. The positional coordinate vector $\mathbf{r}(t) = [x(t)\ y(t)\ z(t)]^{\top}$ represents the tool tip coordinates in the Cartesian coordinate system. Accordingly, the modal transformation is expressed as $\mathbf{U}\mathbf{q}(t) = \mathbf{r}(t)$.

The structural dynamics (the left-hand side of (1)) is assumed to be linear, but the forcing $\mathbf{F}(t, \mathbf{r}_t)$ is a nonlinear and nonsmooth function of past vibrations of the tool. For time-delay system it is common to use the representation with the function segment $\mathbf{r}_t(\theta) \coloneqq \mathbf{r}(t-\theta)$, $\theta \in [0, \tau_{\max}]$ as the state, which defines all past positions of the tool from $t - \tau_{\max}$ up to t, and $\tau_{\max}$ is the largest delay (out of all) that occurs.

For the sake of simplicity and clarity, this study is intentionally limited to regular milling cutters, where Z is the number of equally spaced cutting edges. The coordinate system is oriented in the direction of feed, such that coordinate axis x is parallel to the feed velocity vector $\mathbf{v}_{\mathrm{f}} = [v_{\mathrm{f}}\,0\,0]^{\top}$ (v_{f} is the feed rate or feed speed), and axis z is parallel with the axis of rotation. The angular velocity Ω (rad/s) of the tool is assumed to be constant, and the spindle speed defined in revolution per minute (rpm) can be computed as $n = \Omega\, 60/(2\pi)$. In our context, it is more appropriate from the technological point of view to define and utilize the feed per tooth f_Z, since it is fixed for a measurement setup (but these technological parameter are related as $f_Z = v_{\mathrm{f}}60/(Zn)$). Therefore, the angular position φ_j ($j = 1, \dots, Z$) of each cutting edge point at time instant t along the axial coordinate z can be given as

$$\varphi_j(t, z) = n\frac{2\pi}{60}\,t + (j-1)\frac{2\pi}{Z} - \frac{2z}{D}\tan\gamma, \tag{2}$$

where $D = 2R$ is the nominal diameter, R is the radius of the tool, and γ is the helix angle of the flutes.

The spindle period (the time of one complete revolution of the tool) can be defined as $T \coloneqq 60/n$, and consequently, the tooth passing period as $T_Z \coloneqq T/Z$. Due to the geometric considerations, the possible regenerative delays for regular tools (uniform pitch and identical helix angles) are the multiples of the tooth passing period, that is, $\tau, 2\tau, \dots, Z\tau$, where $\tau \coloneqq T_Z$ is the smallest (nonzero) delay, while the maximum delay $\tau_{\max} \coloneqq Z\tau = T$ matches the spindle period. Specifically, the time delay between an arbitrary tooth j and the previous tooth i can be computed as

$$\tau_{j,i} = \begin{cases} (i-j)\tau, & \text{if } i > j, \\ (i+Z-j)\tau, & \text{if } i \le j, \end{cases} \tag{3}$$

where we take into account that only the past cuts (up to maximum one revolution) have effect on the surface regeneration. Note that $\tau_{j,j} = Z\tau = T$ refers to the time delay corresponding to one complete revolution. For regular tools, maximum $N_\tau = Z$ number of point delays can be distinguished, but not all of them occur necessarily in the equations. The *active delays* that are really affecting the surface regeneration are determined based on the actual CWE (see the delay patterns in Fig. 2). Note that only T-periodic solutions are sought, and the bifurcations beyond this are not in the scope of the paper.

The engagement of the cutting edges are sometimes drastically changed by the tool runout, see Fig. 2 again as an example. In the ideal case, when the runout is omitted ($r = 0$ μm in Fig. 2a), the solution is time-periodic with the principal period being $T_{\mathrm{p}} = T_Z$. The engagements of the edges, the uncut chip thickness h at each teeth, and the delay patterns are all identical and T_Z-periodic, moreover, there is only a single active delay (τ). However, if a minor runout is present (Fig. 2b), then the solutions become instantly T-periodic ($T_{\mathrm{p}} = T$), the delay pattern also changes, and multiple delays occur. In the extreme scenario (Fig. 2c), some cutting edges fly over the workpiece, or can also miss a complete cut due to the relatively high-amplitude vibrations.

Based on the two-parameter model of runout [18], one can approximate the effective radius $R_j(z)$ for each

cutting edge j along the vertical axis as

$$R_j(z) \approx R + \underbrace{r\cos\big((j-1)\frac{2\pi}{Z} - \frac{2z}{D}\tan\gamma - \psi\big)}_{=:\,\Delta r_j(z)}, \tag{4}$$

where $\Delta r_j(z)$ is interpreted as the *relative runout*, measured with respect to the nominal radius R, and ψ is an alignment angle that defines the position of the geometric axis. Alternatively, the relative runout of each cutting edge can be measured individually and used to generalize the model (more relevant for inserted cutters), however, this extension is not considered here.

Based on the geometric considerations up to this point, the so-called geometric uncut chip thickness h_g is approximated as

$$h_{\mathrm{g},j}(t,z,\mathbf{r}_t) \approx \min_{i=1}^{Z} \Big(\mathbf{n}_j^\top(t,z)\Big(\tau_{j,i}\mathbf{v}_\mathrm{f} + \mathbf{r}(t) - \mathbf{r}\big(t-\tau_{j,i}\big)\Big) + R_j(z) - R_i(z)\Big), \tag{5}$$

where $\mathbf{n}_j(t,z) = [\sin\varphi_j(t,z)\ \ \cos\varphi_j(t,z)\ \ 0]^\top$ is the local normal direction of the cutting edge [33], see Fig. 1b. The minimum of the function (5) does not only give the physical uncut chip thickness, but the corresponding delays $\tau_{j,i}$ can also be extracted, which determines the delay patterns and the active delays. It is possible, that this function gives negative values, which are physically not realistic, that is, the edge flies over the surface without cutting when $h_{\mathrm{g},j} < 0$. Consequently, when the tool is not engaging the material, it is considered by the fly-over screen function

$$g_{\mathrm{fo},j}(t,z,\mathbf{r}_t) = \begin{cases} 1, & \text{if } h_{\mathrm{g},j}(t,z,\mathbf{r}_t) > 0, \\ 0, & \text{otherwise.} \end{cases} \tag{6}$$

Moreover, the boundaries of the workpiece are also taken into account, meaning that the entering angle φ_en and exiting angle φ_ex at which the tool can contact the material are defined by the physical process, and mathematically by the radial engagement screen function

$$g_{\mathrm{ri},j}(t,z) = \begin{cases} 1, & \text{if } \varphi_\mathrm{en} < (\varphi_j(t,z) \bmod 2\pi) < \varphi_\mathrm{ex}, \\ 0, & \text{otherwise.} \end{cases} \tag{7}$$

The entering and exiting angles depends on the operation type (up- or down-milling) and on the radial immersion a_e (see Fig. 1b). The joint effect of the different screen functions are considered by

$$g_j(t,z,\mathbf{r}_t) = g_{\mathrm{ri},j}(t,z)\,g_{\mathrm{fo},j}(t,z,\mathbf{r}_t) \tag{8}$$

resulting in the actual physical uncut chip thickness for each tooth by

$$h_j(t,z,\mathbf{r}_t) = g_j(t,z,\mathbf{r}_t)\,h_{\mathrm{g},j}(t,z,\mathbf{r}_t). \tag{9}$$

The cutting force characteristics

$$\mathbf{f}(h) = \begin{bmatrix} f_\mathrm{t}(h) \\ f_\mathrm{r}(h) \\ f_\mathrm{a}(h) \end{bmatrix} \tag{10}$$

describes the cutting force as the function of the uncut chip thickness h, where f_t, f_r and f_a denote tangential, radial and axial characteristics, respectively. These empirical functions and the parameters therein are determined experimentally, often defined in the local edge coordinate system [5]. The resultant cutting force is then transformed into the global Cartesian coordinate system, and can be computed as

$$\mathbf{F}\big(t,\mathbf{r}_t\big) = -\sum_{j=1}^{Z}\int_0^a g_j(t,z,\mathbf{r}_t)\mathbf{T}\big(\varphi_j(t,z)\big)\mathbf{f}\big(h_j(t,z,\mathbf{r}_t)\big)\mathrm{d}z, \tag{11}$$

where the transformation matrix is

$$\mathbf{T}\big(\varphi_j(t,z)\big) = \begin{bmatrix} \cos\varphi_j(t,z) & \sin\varphi_j(t,z) & 0 \\ -\sin\varphi_j(t,z) & \cos\varphi_j(t,z) & 0 \\ 0 & 0 & 1 \end{bmatrix}, \tag{12}$$

and a is the axial depth of cut (axial immersion). For additional material on the topic, we refer to the work of Dombovari et al. [33], and to the references therein.

2.2 Computation of periodic solutions

The equation of motion defined by (1) is generally nonlinear and nonsmooth due to the highly intermittent nature of the milling cutting operation. This poses many computational issues, which can be handled by improved methods. For the proper mathematical treatment of the time-periodic delay-differential equation (TPDDE), the stationary solution $\overline{\mathbf{r}}(t) = \overline{\mathbf{r}}(t+T_\mathrm{p})$, which satisfies (1), must first be determined. Then, the defined variational system around the stationary solution carries the stability properties that are obtained by computing the Floquet multipliers of the associated TPDDE [9,34,35].

There are special scenarios, as mentioned before, such as when the runout is ignored ($r = 0$ μm). In this case the model simplifies a lot, because $T_\mathrm{p} = T_Z = \tau$ (there is only one active delay), and the regenerative term $\overline{\mathbf{r}}(t) - \overline{\mathbf{r}}(t-\tau) = \mathbf{0}$ can be dropped from (5). Although the dynamical system is still nonlinear and nonsmooth, the periodic solution can be determined in a linear manner. Moreover, the CWE is not affected

by the stationary motion, and hence the classical approach is valid. This assumption is what mostly used in the literature.

The exclusion of forced vibrations is not acceptable in the presence of runout, since multiple delays can occur and the periodic solution does not vanish in (5). The asymmetric engagement is elevated further due to the vibrations, which can alter the delay patterns even more, and can change the stability properties, too. Solving the equations in this case require the use of nonlinear computational tools.

The mathematical problem outlined below is well-established in nonlinear systems theory. Research papers, such as the work of Roose and Szalai [36], and standard textbooks, including those by Kuznetsov [37] and Govaerts [38], present efficient techniques that are specifically developed for such models. Here, a relatively simple approach is proposed using finite difference schemes (similarly to the works of Faassen et al. [28] or Wahi and Chatterjee [39]), that keeps the numerical treatment straightforward while still being capable of revealing new topological features.

By formulating Newton's method for this problem, one can create a numerical iterative algorithm that converges to the solution of the equation. To form a fixed-point iteration problem, the nonlinear forcing in (1) is linearized around a trial periodic motion $\overline{\mathbf{r}}_t$, that is,

$$\mathbf{F}\big(t,\mathbf{r}_t\big) \approx \mathbf{F}\big(t,\overline{\mathbf{r}}_t\big) + \Delta\mathbf{F}\big(t,\mathbf{r}_t,\overline{\mathbf{r}}_t\big), \tag{13}$$

where $\mathbf{F}\big(t,\overline{\mathbf{r}}_t\big)$ is already T-periodic and the force variation $\Delta\mathbf{F}$ is linear in $\mathbf{r}_t$ and $\overline{\mathbf{r}}_t$. The variational part can be written as

$$\Delta\mathbf{F}\big(t,\mathbf{r}_t,\overline{\mathbf{r}}_t\big) = \mathbf{A}_0(t,\overline{\mathbf{r}}_t)\big(\mathbf{r}(t)-\overline{\mathbf{r}}(t)\big) + \sum_{l=1}^{N_\tau}\mathbf{A}_l(t,\overline{\mathbf{r}}_t)\big(\mathbf{r}(t-\tau_l)-\overline{\mathbf{r}}(t-\tau_l)\big), \tag{14}$$

where the distinct point delays (for simplicity) are distinguished by τ_l ($l=1,\dots,N_\tau$), and the time-periodic coefficient matrices obtained after the linearization are

$$\mathbf{A}_l(t,\overline{\mathbf{r}}_t) \coloneqq \left.\frac{\partial\mathbf{F}\big(t,\mathbf{r}_t\big)}{\partial\mathbf{r}(t-\tau_l)}\right|_{\mathbf{r}_t=\overline{\mathbf{r}}_t}, \quad \text{and} \tag{15}$$

$$\mathbf{A}_0(t,\overline{\mathbf{r}}_t) \coloneqq -\sum_{l=1}^{N_\tau}\mathbf{A}_l(t,\overline{\mathbf{r}}_t). \tag{16}$$

Here, in (16) $\mathbf{A}_0$ is also referred to as the directional factor matrix, which helps in distinguishing the topologically different cutting operations [40].

For notational convenience, let us define $\tau_0 \coloneqq 0$, corresponding to the non-delayed terms. Then, inserting the linearized forms into (1), employing modal transformation $\mathbf{U}\mathbf{q}(t)=\mathbf{r}(t)$, and simplifications, one can obtain

$$\ddot{\mathbf{q}}(t) + \hat{\mathbf{C}}\dot{\mathbf{q}}(t) + \hat{\mathbf{K}}\mathbf{q}(t) = \mathbf{U}^\top\mathbf{F}\big(t,\mathbf{U}\overline{\mathbf{q}}_t\big) + \sum_{l=0}^{N_\tau}\mathbf{B}_l(t,\overline{\mathbf{q}}_t)\big(\mathbf{q}(t-\tau_l)-\overline{\mathbf{q}}(t-\tau_l)\big), \tag{17}$$

where $\mathbf{B}_l(t,\overline{\mathbf{q}}_t) \coloneqq \mathbf{U}^\top\mathbf{A}_l(t,\overline{\mathbf{r}}_t)\mathbf{U}$.

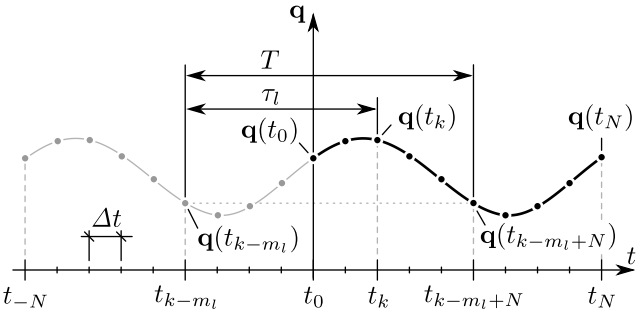

Fig. 3 Discretization of the periodic solution over an equally spaced grid with N intervals.

To formulate the iterative approach using the finite difference schemes, the time-interval $[0,T]$ is divided into N equally spaced segments ($N+1$ points), where $t_0=0$ and $t_N=T$, see Fig. 3. Then, the required derivatives are approximated as

$$\dot{\mathbf{q}}(t_k) \approx \frac{\mathbf{q}(t_{k+1})-\mathbf{q}(t_{k-1})}{2\Delta t}, \quad \Delta t = \frac{T}{N} = t_{k+1}-t_k,$$
$$\ddot{\mathbf{q}}(t_k) \approx \frac{\mathbf{q}(t_{k+1})-2\mathbf{q}(t_k)+\mathbf{q}(t_{k-1})}{\Delta t^2}. \tag{18}$$

The periodicity is guaranteed if we consider for all t that $\mathbf{q}(t+T)=\mathbf{q}(t)$. Therefore, the delayed coordinates are $\mathbf{q}(t-\tau_l)=\mathbf{q}(t_{k-m_l})$, where $m_l=\lfloor\tau_l/\Delta t\rfloor$ (or an even better approximation is a linear interpolation between neighboring points [28]). Since periodicity is assumed, if a function value at negative time is needed ($t_{k-m_l}<0$), then the index is shifted by N, i.e., $\mathbf{q}(t_{k-m_l})=\mathbf{q}(t_{k-m_l+N})$, and it is used instead. In the following, let us define the discretized states as

$$\mathbf{u} = \begin{bmatrix}\mathbf{q}(t_0)\\ \mathbf{q}(t_1)\\ \vdots \\ \mathbf{q}(t_{N-1})\end{bmatrix}, \quad \overline{\mathbf{u}} = \begin{bmatrix}\overline{\mathbf{q}}(t_0)\\ \overline{\mathbf{q}}(t_1)\\ \vdots \\ \overline{\mathbf{q}}(t_{N-1})\end{bmatrix} \big(\in\mathbb{R}^{Nd}\big), \tag{19}$$

where only the points up to t_{N-1} are needed, since $\mathbf{q}(t_N)=\mathbf{q}(t_0)$ is the periodicity constraint. The discretization yields N number of discrete matrix equations (consequently, Nd scalar equations, where d is the number of modes), which are arranged in a large

(but sparse) matrix equation. The corresponding vectors ($\mathbb{R}^{Nd}$) and matrices ($\mathbb{R}^{Nd\times Nd}$) are formulated as

$$\mathbf{Q}(\mathbf{u}) = \begin{bmatrix} \mathbf{U}^\top \mathbf{F}\big(t_0, \mathbf{P}\mathbf{u}\big) \\ \mathbf{U}^\top \mathbf{F}\big(t_1, \mathbf{P}\mathbf{u}\big) \\ \vdots \\ \mathbf{U}^\top \mathbf{F}\big(t_{N-1}, \mathbf{P}\mathbf{u}\big) \end{bmatrix}, \quad \mathbf{P} = \begin{bmatrix} \mathbf{U} & & \\ & \mathbf{U} & \\ & & \ddots \\ & & & \mathbf{U} \end{bmatrix}, \tag{20}$$

$$\mathbf{D} = \begin{bmatrix} \mathbf{d}_0 & \mathbf{d}_1 & & & \mathbf{d}_{-1} \\ \mathbf{d}_{-1} & \mathbf{d}_0 & \mathbf{d}_1 & & \\ & \mathbf{d}_{-1} & \mathbf{d}_0 & \ddots & \\ & & \ddots & \ddots & \mathbf{d}_1 \\ \mathbf{d}_1 & & & \mathbf{d}_{-1} & \mathbf{d}_0 \end{bmatrix}, \quad \begin{aligned} \mathbf{d}_{-1} &= \tfrac{1}{\Delta t^2}\mathbf{I} - \tfrac{1}{2\Delta t}\hat{\mathbf{C}}, \\ \mathbf{d}_0 &= -\tfrac{2}{\Delta t^2}\mathbf{I} + \hat{\mathbf{K}}, \\ \mathbf{d}_1 &= \tfrac{1}{\Delta t^2}\mathbf{I} + \tfrac{1}{2\Delta t}\hat{\mathbf{C}}, \end{aligned} \tag{21}$$

$$\mathbf{B}(\overline{\mathbf{u}}) = \sum_{l=0}^{N_\tau} \left[\begin{array}{ccc|ccc} & \cdots & & N-m_l & & \\ & & & & & \\ \ddots & & & & & \\ & & \mathbf{B}_l(t_{N-1}, \overline{\mathbf{u}}) & & & \end{array}\right. \left.\begin{array}{ccc} N-m_l+1 & N-m_l+2 & \cdots \\ \mathbf{B}_l(t_0, \overline{\mathbf{u}}) & & \\ & \mathbf{B}_l(t_1, \overline{\mathbf{u}}) & \\ & & \ddots \end{array}\right], \tag{22}$$

where the empty spaces in the matrix entries are filled up with zeros (and the matrix is circularly banded). Also note that matrix $\mathbf{B}$ is built up from submatrices $\mathbf{B}_l(t_k, \overline{\mathbf{u}})$, where the nondelayed elements $\mathbf{B}_0$ ($\tau_0 = 0$ and $m_0 = 0$) remain in the main diagonal, and all other bands are circularly shifted from the diagonal element to the left by m_l blocks depending on the delays τ_l.

Using the discretized forms above, a nonlinear equation ($\mathbf{G}(\mathbf{u}) = \mathbf{0}$) and its linear approximation based on (17) can be written as

$$\begin{aligned} \mathbf{G}(\mathbf{u}) &= \mathbf{D}\mathbf{u} - \mathbf{Q}(\mathbf{u}) \\ &\approx \mathbf{D}\mathbf{u} - \mathbf{Q}(\overline{\mathbf{u}}) - \mathbf{B}(\overline{\mathbf{u}})(\mathbf{u} - \overline{\mathbf{u}}). \end{aligned} \tag{23}$$

Since the fixed point of (23) is yet unknown, it can be reformulated into an iteration scheme as

$$\begin{aligned} \mathbf{u}^{(i+1)} &= \mathbf{u}^{(i)} - \big(\mathbf{J}(\mathbf{u}^{(i)})\big)^{-1}\mathbf{G}(\mathbf{u}^{(i)}) \\ &= \mathbf{u}^{(i)} - \big(\mathbf{D} - \mathbf{B}(\mathbf{u}^{(i)})\big)^{-1}\big(\mathbf{D}\mathbf{u}^{(i)} - \mathbf{Q}(\mathbf{u}^{(i)})\big), \end{aligned} \tag{24}$$

where $\mathbf{J}$ is the Jacobian of $\mathbf{G}$. The method converges to $\overline{\mathbf{u}}$ as $i \to \infty$, but it should be stopped if the error reaches a limit. For starting, $\mathbf{u}^{(0)} = \mathbf{0}$ may be used, and it often works well, however, it may fail to converge if multiple solutions close to each other exist. Note that at every ith step, the discretized state $\mathbf{u}^{(i)}$, vector $\mathbf{Q}(\mathbf{u}^{(i)})$ and matrix $\mathbf{B}(\mathbf{u}^{(i)})$ need to be updated considering the change of the delay patterns and variations in the CWE.

Equation (24) is the core of the iteration process, which is either used to find a stationary solution at one specific point on the stability chart, or it can be implemented in a continuation method. In this work, the pseudo-arclength method in utilized [41], and the solution curve is followed along the spindle speed n or the depth of cut a. The algorithm is presented briefly in Appendix A. To compute the Floquet multipliers μ, which characterize the local stability of the periodic motion, the semi-discretization method is employed (see Appendix B), however, more advanced numerical techniques may also be used as alternatives.

3 Numerical study and experiments

Experimental validations are performed on a single-degree-of-freedom (SDoF) test rig, see Fig. 4a. The dynamical response can be characterized well by a single dominant vibration mode in direction y (Fig. 4b), while the feed direction x (and also z) can be assumed rigid. The corresponding modal parameters are given in Tab. 1. (the unnormalized mode shape vector is $\mathbf{U} = \mathbf{p}/\sqrt{m}$). The use of this test rig makes the study more suitable for presentations, and reduces the impact of uncertainties. Moreover, the displacements (accelerations) can directly be measured on the flexure, which would not be possible at the tool tip during operation.

A dynamometer was also placed under the workpiece, which was used to measure cutting forces during the tests. In order to eliminate the inertial effects, a dynamic compensation technique (filtering) was utilized [32]. Therefore, both the measured cutting forces and stationary periodic solutions can be compared to the predictions.

The cutting force characteristics were identified from preliminary measurements, and the values of runout magnitude and angle were identified from the fitted cutting forces directly [32]. The workpiece was made of aluminum (AL2024-T351) for which exponential characteristics [42] were assumed in the form

$$f_j(h) = K_{\mathrm{c},j} h + K_{\mathrm{e},j}(1 - \mathrm{e}^{-E_j h}), \quad j = \mathrm{t}, \mathrm{r}, \mathrm{a}, \tag{25}$$

see Fig. 4c with the actual parameters. The tool-, process- and workpiece data used in this study are listed in Tab. 2. Note that the force characteristics is continuous at $h = 0$ (i.e., $f_j(0) = 0$), which helps the convergence of the numerical iterations. However, the steep

Table 1 Reference modal parameters of the workpiece.

ω_n (Hz)	ζ (%)	m (kg)	$\mathbf{p}$ (m/m)
247.405	0.8921	2.5045	$[0\ 1\ 0]^\top$

Table 2 Technological data of the tool and process parameters.

tool data		process data		workpiece data
type	Tivoly G9425160 solid carbide end mill	feed per tooth	$f_Z = 0.05$ mm/tooth	$f_j(h) = K_{c,j}h + K_{e,j}(1 - e^{-E_j h})$
		radial depth of cut	$a_e = 6$ mm	$K_{c,t} = 820.1$ N/mm^2
		process type	down-milling (37.5%)	$K_{e,t} = 12.46$ N/mm
tooth number	$Z = 3$			$E_t = 704.5$ 1/mm
diameter	$D = 16$ mm			$K_{c,r} = 45.37$ N/mm^2
helix	$\gamma = 30°$			$K_{e,r} = 18.37$ N/mm
runout magnitude	$r = 17.46$ μm			$E_r = 217$ 1/mm
runout angle	$\psi = 112°$			$K_{c,a} = 134.1$ N/mm^2
				$K_{e,a} = 80.95$ N/mm
				$E_a = 1.281$ 1/mm

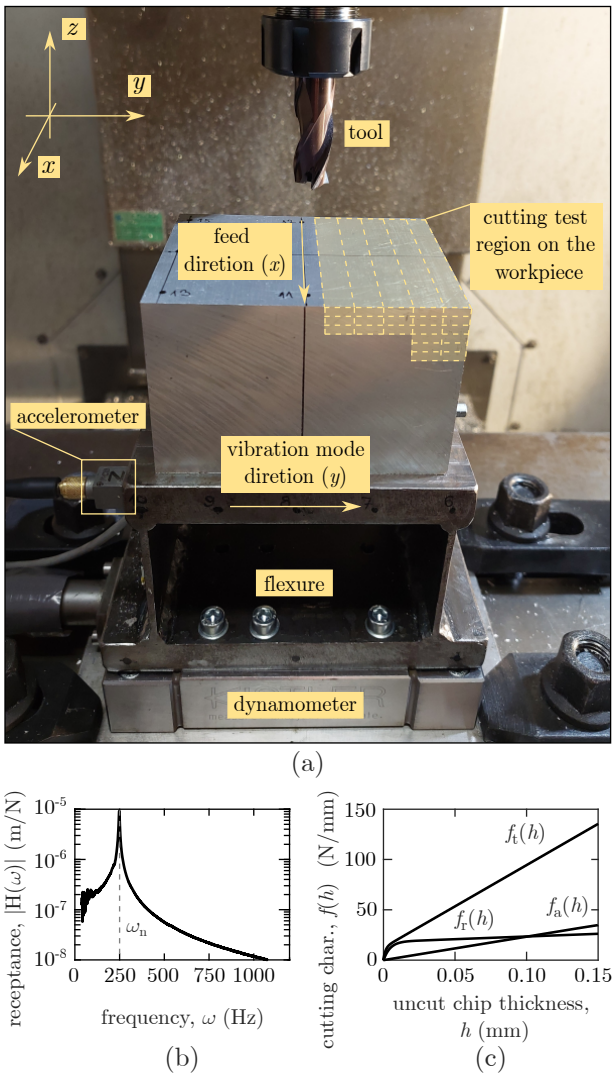

Fig. 4 Experimental setup on a test rig. The flexure is compliant in direction y, which is perpendicular to the feed direction x. Accelerometers and dynamometer are used to measure compensated cutting forces during the tests [32]. (a) SDoF test rig, (b) frequency response function in the mode direction, (c) identified cutting characteristics corresponding to the tool-workpiece combination.

slopes at very small h require higher resolution in the discretization to avoid the numerical instabilities and approximate sufficiently the characteristic multipliers. For shifted discontinuous characteristics ($f_j(0) \neq 0$), in general, the state must be approximated by piecewise-smooth polynomials [43], which makes the numerical implementation significantly more complex.

In this study, a three-fluted milling cutter ($Z = 3$) was used, which showed unexpected behavior under certain technological parameters in earlier experiments [32]. Unusual stable attracting solutions were observed on the SDoF test rig in down-milling (DM) operations, that is, under conditions with a positive mean directional factor in our case [40]. By applying a continuation technique (see Appendix A), we are able to uncover new solution branches. Understanding these topological features lays the groundwork for analyzing more complex multiple-degrees-of-freedom (MDoF) models and general milling cutters. While the mathematical framework presented here extends naturally to MDoF systems—where similar bifurcation diagrams can be observed—the interaction between modes introduces significant complexity. Therefore, this case study focuses on the SDoF case only.

3.1 Predicted stability lobe diagrams

First, the traditional stability chart is presented in Fig. 5a, where the runout is set to zero, i.e., $r = 0$ μm. The corresponding modal parameters and technological data are all given in Tab. 1 and Tab. 2, while the resolution of the discretization was $N = 300$ (same N is used for the semi-discretization method). To accelerate the computation and achieve a high-resolution chart, a bisection method was applied following the approach in [44]. The initial grid size was 100-by-10 points, and four bisection steps were performed, effectively resulting in a refined grid of 1600-by-160 points. The green shaded area indicates the domain of the stable technological parameters, while the red is unstable. Note

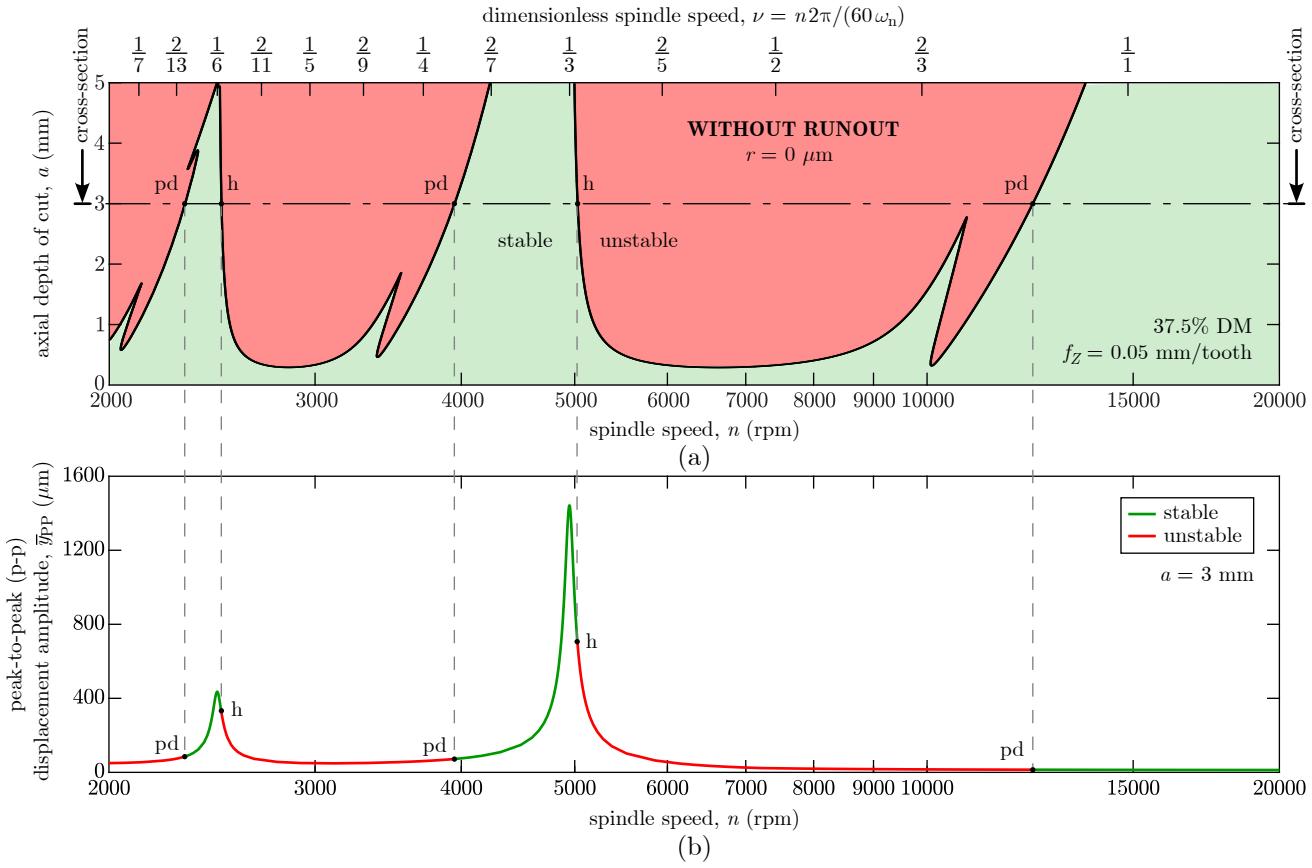

Fig. 5 Stability lobe diagram without runout. (a) Domain of stable and unstable technological parameters. (b) Peak-to-peak displacement amplitudes of the periodic solution at $a = 3$ mm axial depth of cut.

that the horizontal axis (spindle speed n) is in logarithmic scale, for visualization purposes. The stability of the periodic solution at the boundaries (black curve) is lost through either Hopf- (h) or period-doubling (pd) bifurcation. In order to see how the periodic solutions are changing along the spindle speed, the depth of cut $a = 3$ mm is selected, and the continuation method was utilized. Due to visualization difficulties, only the peak-to-peak displacement amplitudes were plotted ($y_{PP} := \max \overline{y}(t) - \min \overline{y}(t)$). There are definitely many other factors (peak force, average force, tool edge engagement time, surface quality, surface location error, etc.) which can be very different at selected points, but this cannot be fully studied in this work. Here, we most importantly concentrate on the existence of the captured solutions and on the validation of the dynamical model.

In Fig. 5a, the top horizontal axis is the dimensionless spindle speed $\nu = n\,2\pi/(60\omega_n)$, which helps to localize resonances, where one harmonic of the forcing is close to the natural angular frequency ω_n of the test rig. The vibration amplitudes are high at the classical resonances, where $\nu \approx 1/(kZ)$, $k \in \mathbb{N}$, see Fig. 5b.

The stability chart gets fundamentally different if runout ($r = 17.46$ μm based on measurement) is taken into account, see Fig. 6a. Again, the stability chart was computed using a bisection method [44], where all Newton iterations were initialized from the trivial solution ($\mathbf{u}^{(0)} = \mathbf{0}$). It is important to note that this may not guarantee the convergence if multiple solutions exist, which resulted sometimes scattered boundaries. In some cases only the stationary solution closest to the initial guess was found, the others were consequently lost. This can make the evaluation of the charts complicated, the diagram is not complete (!) in the sense that some possible stable domains remained hidden. Note that the gray curve corresponds to the stability boundary of the model without runout, so that the difference between the two charts can be seen. Even far from resonances, the boundaries are slightly shifted. Also note that the markers indicate measurement points, which show excellent agreement with predictions, the details are deeply discussed later in subsec. 3.2.

Figure 6b shows the computed periodic solutions (only the peak-to-peak displacement amplitudes y_{PP}) obtained by the single-parameter continuation approach. There are many unusual phenomena appearing, especially at regions R1/R2/R3 highlighted by yellow. At region R1 an isolated branch of solutions is captured,

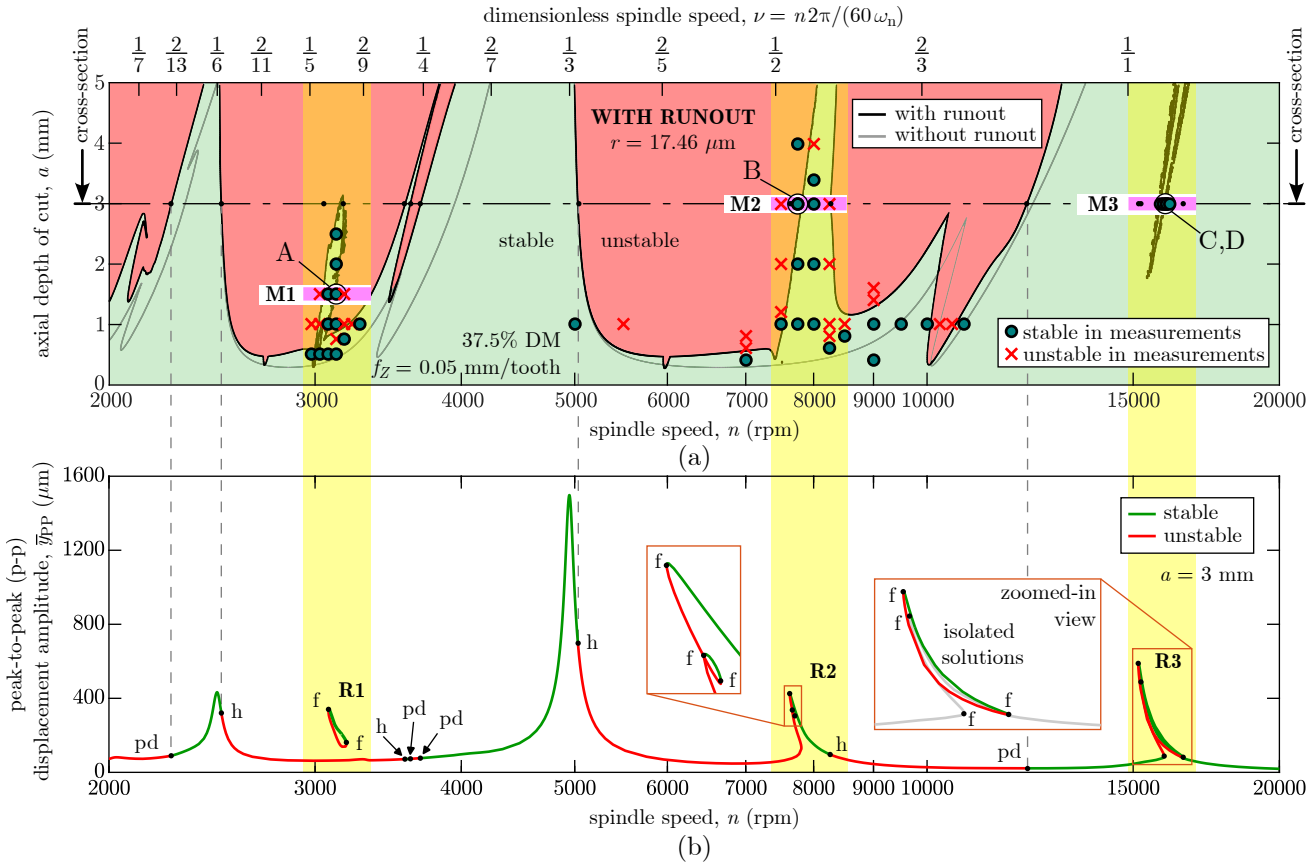

Fig. 6 Stability lobe diagram with runout. (a) Domain of stable and unstable technological parameters. (b) Peak-to-peak displacement amplitudes of the periodic solution at $a = 3$ mm axial depth of cut.

where the two limit points are the fold points (f) of the curves. At these limit points there exists a multiplier $\mu = 1$ (cyclic-fold was observed in other publications [29,32]). At region R2, the branch is not detached, but two stable periodic solutions can coexist at a very narrow spindle speed region. Most surprisingly, at region R3 the nonlinear system has three stable and two unstable solutions within a relevant range of spindle speeds (note the logarithmic scale). A pair of stable and unstable solutions similarly to region R1 are detached, which is hard to capture and visualize. In Fig. 6b, the zoomed-in views magnify the solution curves to see the overlapping branches (details are discussed later in subsec. 3.3).

The three-dimensional views of the highlighted regions (R1/R2/R3) are shown in Fig. 7. In order to see better the transition, the continuation method was restarted at different depth of cuts. In Fig. 7a, the separation of the isola is not visible, it happens slightly below $a = 1$ mm. At higher depth of cuts, the vibration amplitudes increase and the isole move farther from the low-amplitude unstable connected branch of solutions. In experiments, the stable solutions on the isola can be mistaken for unstable behavior (e.g., period-n bifurcations [45,27]) due to the suddenly different dynamical response. However, from a practical standpoint, it is not straightforward to determine whether such behavior is stable or unstable. This may be one reason why such solutions are not reported in many case studies.

In Fig. 7b, the inner loop is being formed around $a = 2$ mm, above which mathematically two stable solutions can be distinguished. However, this region is very small, the corresponding displacement amplitudes are high, and the CWE may be very different compared to the ideal case. Very often fly-overs and missed cuts are present, which may not be technically favorable.

In Fig. 7c, due to the high-amplitude resonant vibrations again, the loss of contact between the workpiece and tool increases, leading to the formation of new periodic orbits. As mentioned before, a separated isola is also found here, resulting in at least five distinct solutions for a specific spindle speed (16000 rpm). However, the descriptions in this region differ somewhat from the others. The machining process is originally stable, and no particularly unfavorable behavior was expected beforehand. The cutting operation remains stable (even after transitioning from one solution to another), but the switched CWE can be significantly different, which

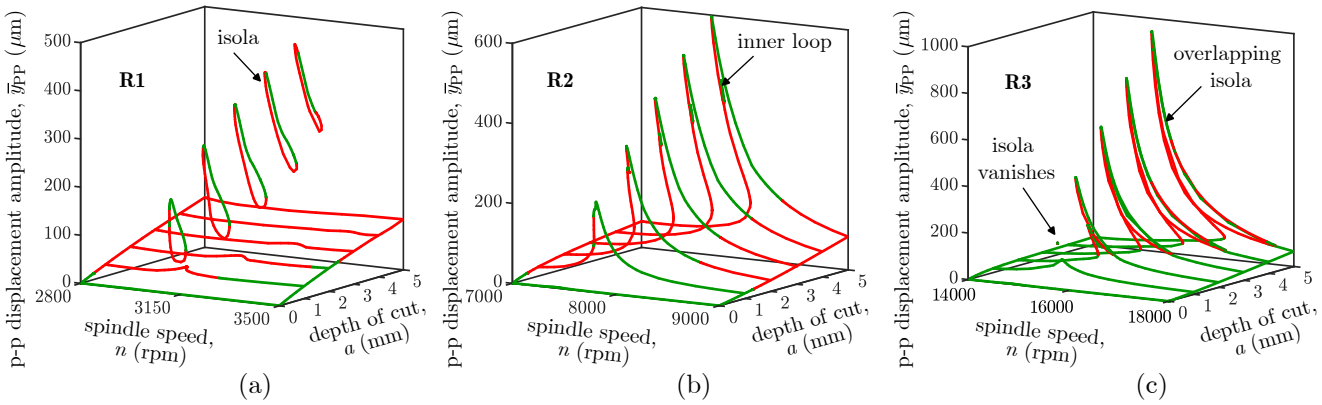

Fig. 7 Peak-to-peak displacement amplitudes at the selected spindle speed regions and at different depth of cuts. (a) R1, (b) R2, (c) R3.

again has important technical implications. Since the numerical approach cannot tell which solution is more likely to attract the trajectories in time during real operations, some experiments need to be conducted.

Based on the various stationary solutions observed in Figs. 6 and 7, it is important to emphasize the technical challenges associated with continuous operation under resonant vibration conditions. On the one hand, the vibrations are high, which should be tolerated by the machine and by its components. The tool cutting edge engagements are very distorted, some teeth may be partly flying, while others cut more material than expected. On the other hand, tool life is a critical factor, it should be carefully considered, and some stationary motions may rather be avoided. Moreover, surface quality and surface location error (SLE) [46] should also be investigated in the future to see how it changes at different speeds. To conclude, even though that the solutions are T-periodic and stable mathematically, some high depth of cuts or resonant spindle speed regions may not be favored in real applications.

3.2 Chatter tests

The highlighted regions (R1/R2/R3) in Fig. 6 present new unexpected solutions. The measurement points where the stability chart was tested are indicated on Fig. 6a, where the green circles are stable and red crosses are unstable. This represents a typical qualitative comparison of stability (i.e., stable vs. unstable), but it does not reflect the quantitative accuracy of the prediction. Since it is too condensed to present all results from point by point, only a few relevant tests were selected at measurement lines M1/M2/M3 (colored by magenta), see Fig. 6a. Note that similar experiments were presented in previous works [31,32] for different technological parameters, but without the close investigation of multistable regions.

One of the biggest issue of the experimental test rig is the change of the physical mass of the workpiece, which decreases as the material is being removed (and sometimes the block is also replaced). The stability chart is drifting from test to test, and therefore the dynamical parameters must be updated continuously. In the next figures (in order to keep the predictions as accurate as possible), the actual updated modal parameters are used, which are given in Tab. 3. These modal parameters are fitted before conducting new chatter tests, and are slightly different from the reference parameters given in Tab. 1, but the charts remain qualitatively the same.

The post-processed measured force signals, and the periodic solutions are shown in Fig. 8. Note also that at these measurements, the stable points are relevant only (unstable orbits cannot be measured, but they can be used to validate the boundary of stability). The peak-to-peak displacement amplitudes of the stable measurement points at the different setups are shown in panels (a)-(c). The force signals including the entering and exiting events, and some zoomed-in views are shown in panels (d)-(f). In order to carefully compare the measurements to predictions, the periodicity of the signal was accurately identified, and the resampled time-periodic quantities (forces and displacement) are all plotted in panels (g)-(j). In the last panels (last three rows), the

Table 3 Updated modal parameters of the workpiece for the individual chatter tests (M1/M2/M3).

test	ω_n (Hz)	ζ (%)	m (kg)	$\mathbf{p}$ (m/m)	a (mm)
M1	250.971	0.8583	2.4107	$[0\ 1\ 0]^\top$	1.5
M2	247.405	0.8921	2.5045	$[0\ 1\ 0]^\top$	3.0
M3	259.516	1.0763	2.1701	$[0\ 1\ 0]^\top$	3.0

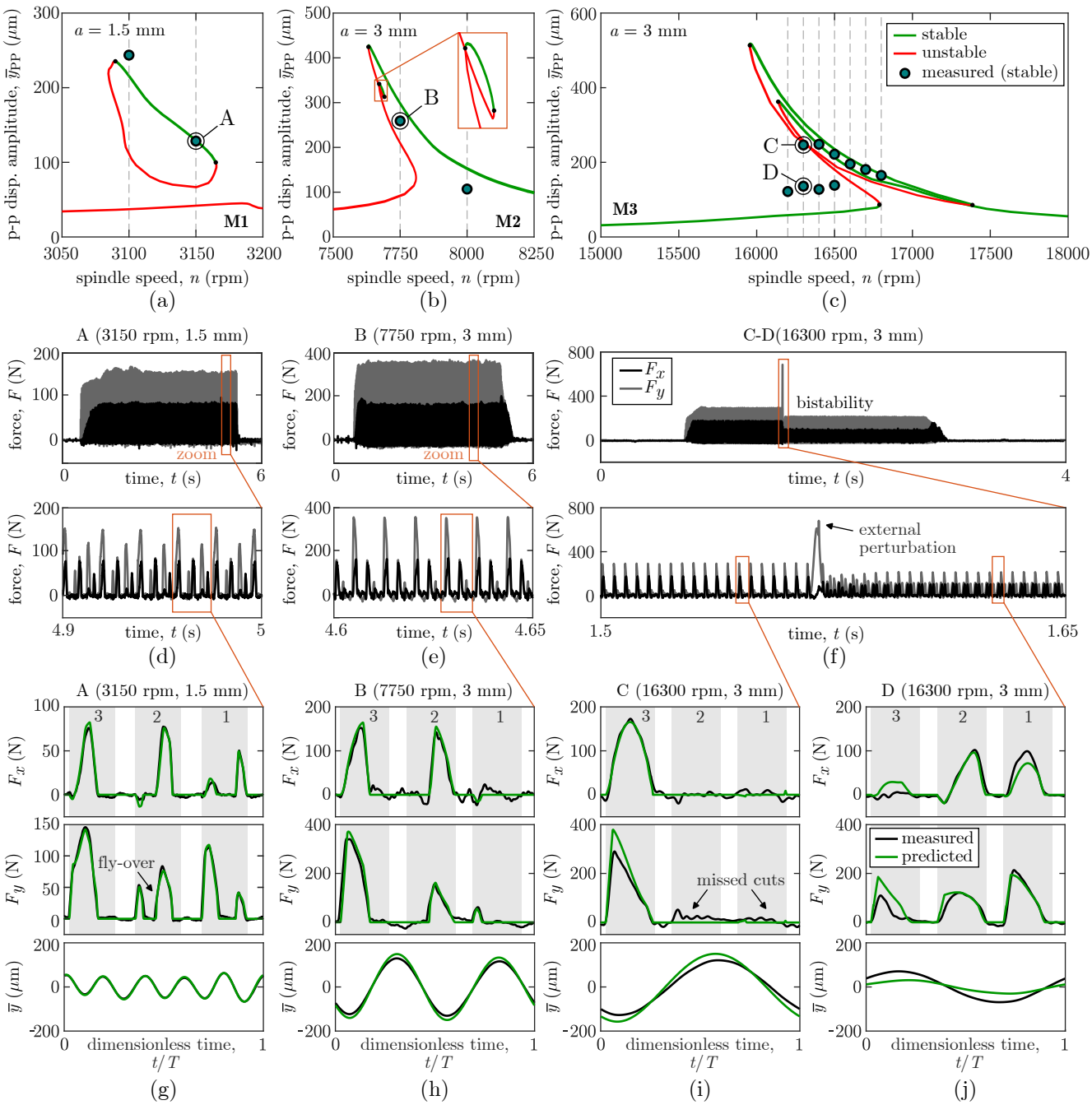

Fig. 8 Detailed measurements at selected points along the stability chart. (a-c) Peak-to-peak displacement amplitudes at measurement lines M1/M2/M3. (d-f) Complete measured force signals in time and some zoomed-in views. (g-j) Comparison of measured and prediction periodic force and displacement signals (black is measured and green is predicted). The gray-shaded areas represent the possible time intervals during which each cutting edge may engage with the workpiece.

black curves are the measured, while the green curves correspond to the computed stable periodic motions.

Sample points picked along measurement lines M1 and M2 are shown in Fig. 8ab. The predictions at points A and B show both qualitatively and quantitatively excellent agreement with predictions (Fig. 8gh). It can be stated that the stable stationary solutions captured in the measurements are very likely identical to what the model with runout predicts.

Figure 8c is a special example from many aspects. Numerical calculations could reveal that multiple stable solutions (three stable) coexist in the spindle speed region circa 16200–16800 rpm. Nevertheless, measurements initiated with a smooth engagement of the tool with the workpiece tend to drive the system toward

stable periodic solutions of higher amplitude. This is counter-intuitive, as one might expect that the transients occurring during the entry would last long enough for the system to eventually settle onto the lower-amplitude solution. The only way the lower-amplitude motion could be observed was through an external perturbation. During the cutting test, approximately 1 second after the entering into the material, the test rig was hit slightly in direction y by a hammer. A time-signal is shown in Fig. 8f. As it can be seen the cutting process is stationary before the perturbation, but the cutting force peak is relatively high. After impacting the workpiece, the forces become smaller and more dense, meaning that the CWEs before and after the impact are very different. It can also be seen that the motion is stationary until the process is finished, so both are stable. These different periodic motions (at points C and D), and the corresponding measured and predicted force signals are presented in Fig. 8ij. The forces show again excellent agreement, it is also visible that the high-amplitude motion corresponds to nearly a single-tooth cutting operations (C), while in the other case three teeth are cutting (D).

Not all impacts lead to a shift between stationary solutions, sometimes the system returns to the original periodic motion. The issues of multistability in time-delay systems, the effect of initial states, and the visualization difficulties of the basin of attraction were discussed in the work of Yan et al. [47]. In that study, the so-called stochastic basins of attraction are computed, which can approximate the probability of a given initial state going to a specific attractor by means of numerical simulations. However, in the experiments, the time instant and energy level of the impact should be designed well if we want to guarantee the jump between the designated solutions, but this is practically infeasible. The multistable behavior during the cutting tests was observed three times at different speeds (Fig. 8c), and approximately half of the impacting test could shift the stationary motion and clearly reveal bistability.

3.3 Remarks on multistability

Multistability worth a deeper investigation, as this presented topic (in the presence of tool runout) has not been observed in other technical reports before. Bistability is often referred to the unsafe zone near the stability boundary (subcritical Hopf-bifurcation), where small perturbation may lead to jump to a different steady-state solution with higher amplitude (quasiperiodic or chaotic) [48]. In this case, although the phenomenon looks similar, it is very different from the mathematical point of view. The multistability in this

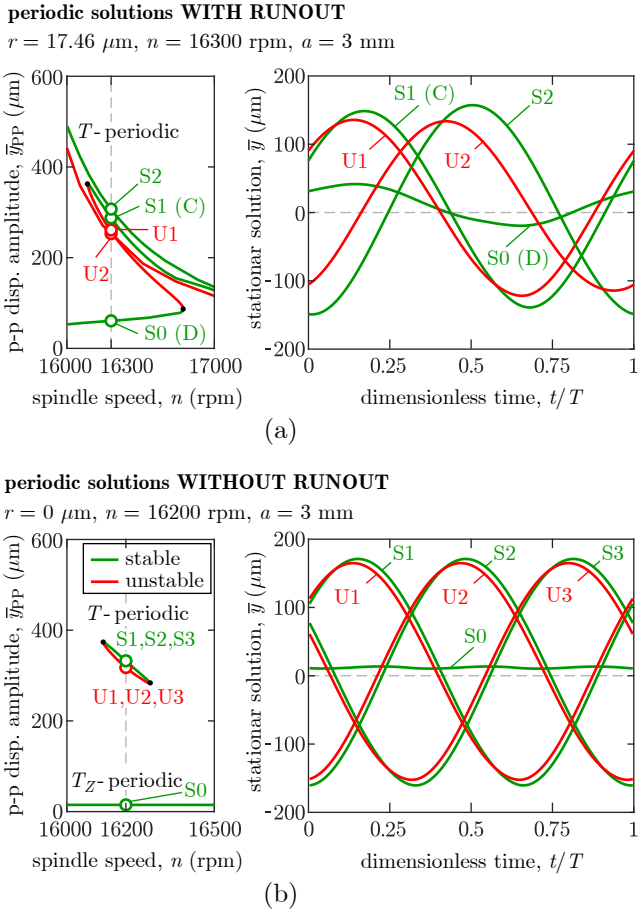

Fig. 9 Stable and unstable periodic solutions. (a) Multiple periodic solutions predicted in the case study (Fig. 8ij) in the presence of runout. (b) Ideal configuration without runout ($r = 0$ μm), where high-amplitude solutions (S1/S2/S3 and U1/U2/U3) are identical and only differ by a symmetric phase shift.

work occurs due to the symmetry breaking effect, where slightly different periodic solutions can belong to very different CWEs, but all of them has the same principal period.

The experimental case study showed the existence of the bistable region, however, the structure suggests that more hidden solutions can exist. In order to understand it better, all stable and unstable periodic solutions are visualized in Fig. 9a, which correspond to the measurement setup M3. The low-amplitude solution S0 (D) belongs to the motion, where all teeth are engaged, but slightly differently, see Fig. 8j. As opposed to this, the high-amplitude solution S1 (C) belongs to the motion, where one tooth is dominant only, and it removes most of the material like a single-tooth cutter, see Fig. 8i. The difference between the observed solution S1 and unobserved S2 (Fig. 9a) is very minor, meaning that both corresponds to similar CWEs, but the dominant tooth is different. It insists that there may exist a third

solution, which is shifted by the phase $2\pi/Z$. However, starting iterations from phase-shifted initial functions did not converge. Therefore, the runout was reduced and the search of the periodic solutions was restarted to reveal the third hidden solution. Surprisingly, the next periodic solution was only captured when the runout was almost disappearing ($r \approx 0$ μm). Aside from the low-amplitude T_Z-periodic regular motion, three stable and three unstable T-periodic solutions can coexist in the runout-free scenario, which only differ by symmetric phase shifts, see Fig. 9b. It means that even in the ideal configuration ($r = 0$ μm), a multistable region can exist, where one tooth is dominant during cutting.

The observation of the multistable region may have only a theoretical importance. If one checks the solutions in Fig. 9b more carefully, it can be observed that the (three) isole are relatively narrow, but not unrealistic (200 rpm wide), while the unstable orbits (U1/U2/U3) are very close to the stable ones (S1/S2/S3). Therefore, even a slight perturbation may repel the trajectories from S1/S2/S3, until S0 is reached. Still, it is not the case in the presence of runout (Fig. 9a), where the topology changes, and the periodic orbits are well separated from each other in the state space. This is the reason why two stable motions are captured during the experiments (the third remained hidden, but the fourth does not even exist), see Fig. 8ij.

In order to get an even deeper insight into the dynamics in the multistable regions, the effect of runout was investigated in Fig. 10. The other technological parameters (Tab. 2) and modal parameters (M3 in Tab. 3) were kept the same. Once a high-amplitude solution was found, the search of the next periodic orbit was initiated from a phase-shifted solution ($2\pi/Z$). If the initial guess was close enough, then the closest point on the isolated solution branch could be found. Repeating this iteration for different runout values, the branches in Fig. 10 could be computed. First, it is recommended to start with a higher runout value ($r = 15$ μm in Fig. 10a), as at least one high-amplitude solution exists on the connected branch and one additional was found by phase-shifted iterations. Then, the iterated solutions were kept, the runout was reduced and the modified solutions were determined (the isola was shrinking). It can be seen that at $r = 5$ μm (Fig. 10b), the elongated curve is already detached, and two isole are formed. Reducing the runout further, at around $r = 0.5$ μm (Fig. 10c), the third missing branch can also be found, yielding three unique, but very similar solutions. To see the complete picture, the last panel shows again the runout-free scenario ($r = 0$ μm in Fig. 10d), where the three isole overlap, and the periodic solutions differ only by a symmetric phase shift $2\pi/Z$ (Fig. 9b).

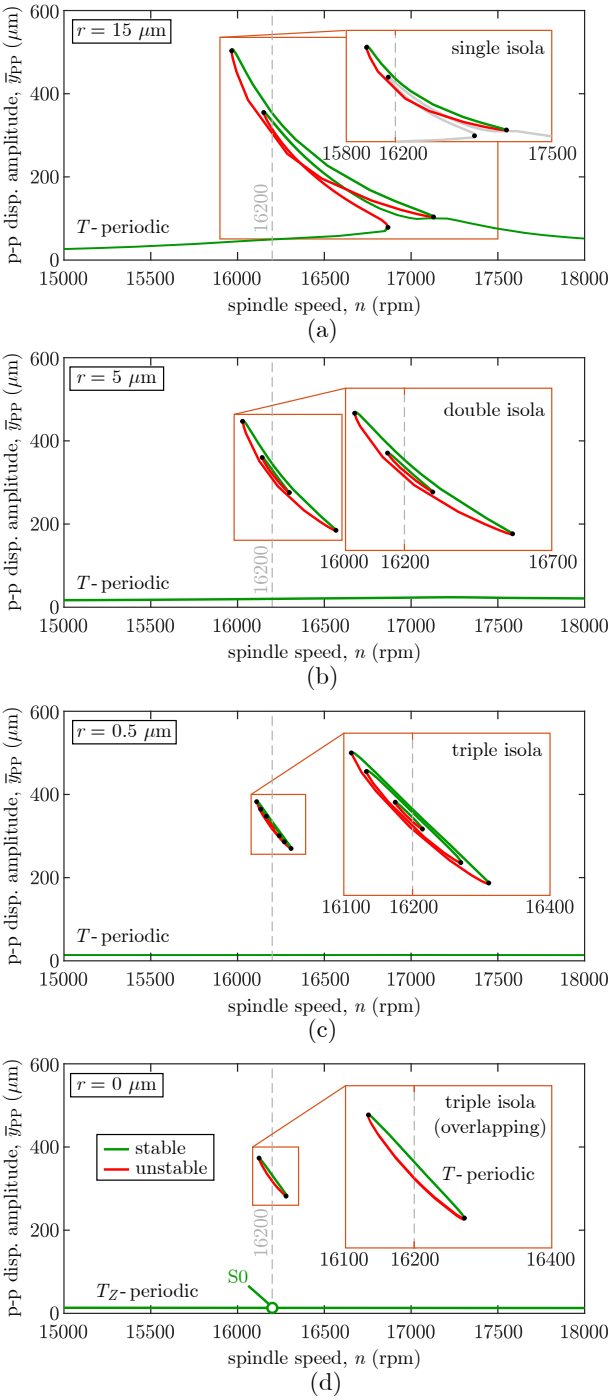

Fig. 10 Effect of runout on the topology of multiple solutions. (d) $r = 15$ μm, (c) $r = 5$ μm, (b) $r = 0.5$ μm, (a) $r = 0$ μm.

Note again that on one hand, the technical issues related to the highly distorted CWEs may reduce the practical importance of these periodic motions. On the other hand, it is possible that the uncertainties lead to the collapse of these solutions, or stochastic resonance effect [49] can also lead to instability even if the deterministic system is stable. Therefore most of these solu-

tions are either just theoretical, unreachable, or should rather be avoided for practical reasons. Still, as it was showed in this study, we cannot always guarantee that unfavorable situations do not arise, and we can unintentionally select technological parameters, where bistability occurs. Even transient effects (start of the cutting) can trigger high-amplitude oscillations, which survives until the end of the operation.

4 Conclusion

The presence of runout introduces significant complexity in the mathematical treatment of milling dynamics. The stability charts cannot be computed accurately in the regular ways due to the involvement of multiple solutions. Instead, advanced techniques (such as path-following methods) must be utilized to capture all possible periodic orbits located on a connected branch.

The detailed analysis of the nonlinear dynamical system revealed that multistabe regions can exist even without runout, which was not addressed before. The newly discovered isolated solutions correspond to high-amplitude periodic motions, where the actual cutter-workpiece engagements (CWE) are significantly distorted compared to the ideal runout-free scenario. These behaviors are usually unfavorable from the technical point of view due to the unequal chip load and vibrations, but they cannot be surely avoided in real applications.

With increasing the runout, the edge engagements become more interrupted, but a richer dynamics can be observed. Runout may account for many of the measurement discrepancies reported in the past, which could not be explained by other means. Bistability observed in experiments is one example, where stability classification methods can be uncertain. Depending on the initial conditions (transients), the trajectories may converge to alternative orbits, which raises new technical problems, too. It is often viewed as post-bifurcation motion (such as period-n chatter), but mathematically there is no regular bifurcation at all (e.g., from primary to secondary solutions), which makes evaluations difficult.

Distinguishing between different periodic motions is essential, yet it remains challenging to separate mathematically stable stationary solutions from those that are practically unfavorable, despite their theoretical stability.

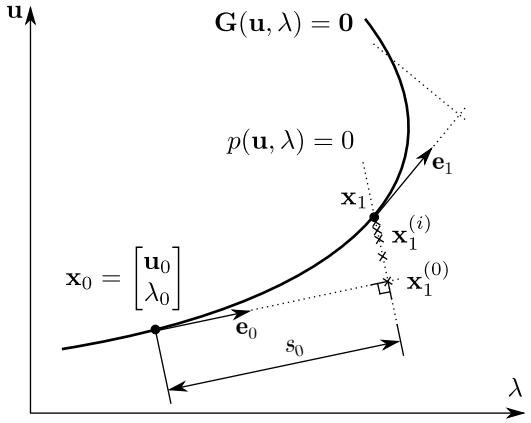

Fig. 11 Illustration of the pseudo-arclength method.

Author contributions

David Hajdu performed the experiments, analyzed the data, developed the programming code, generated the figures, and wrote the manuscript.

Funding

The research reported in this paper and carried out at BME has been supported by the Hungarian National Research, Development and Innovation Office (NKFI-KKP-133846).

This paper was supported by the János Bolyai Research Scholarship of the Hungarian Academy of Sciences.

A Continuation of periodic solutions using the pseudo-arclength method

In this work, the favored pseudo-arclength method presented by Keller [41] is applied (see Fig. 11), which is well-known and technical issues are widely studied in textbooks [37,38] and in scientific papers [50,51], too. This paper aims to present the new typologies and structures of milling stability charts, and therefore the continuation method is only introduced briefly, at the level of understanding the basic concept. The reader is encouraged to bridge the gap by either utilizing existing commercial software—such as MATCONT [52], PDDE-CONT [53], or DDE-Biftool [54]—or by developing and implementing more advanced techniques.

The most important step is to trace the solution $\mathbf{u}$ of the nonlinear equation $\mathbf{G}(\mathbf{u}, \lambda) = \mathbf{0}$ along one of the technological parameters denoted by λ (such as the spindle speed n or depth of cut a). The technique illustrated in Fig. 11 shows how the solution curve $\mathbf{G}$ is followed even beyond the turning point (limit point or fold point). First, a prediction step is made from a starting point $\mathbf{x}_0 = \mathrm{col}(\mathbf{u}_0, \lambda_0)$ along the tangent $\mathbf{e}_0 = \mathrm{col}(\mathbf{e}_{0,\mathbf{u}}, e_{0,\lambda})$ with initial stepsize s_0, then corrections are made on a hyperplane p normal to it using Newton's method.

The defining system of equations are formulated as

$$\mathbf{G}(\mathbf{u},\lambda)=\mathbf{0},$$
$$p(\mathbf{u},\lambda)\coloneqq \mathbf{e}_{0,\mathbf{u}}^{\top}(\mathbf{u}-\mathbf{u}_0)+e_{0,\lambda}^{\top}(\lambda-\lambda_0)-s_0=0. \tag{26}$$

To ease the notation, the compact form is written as

$$\mathbf{H}(\mathbf{x})\coloneqq\begin{bmatrix}\mathbf{G}(\mathbf{x})\\ \mathbf{e}_0^{\top}(\mathbf{x}-\mathbf{x}_0)-s_0\end{bmatrix}=\mathbf{0},\quad \mathbf{x}\coloneqq\begin{bmatrix}\mathbf{u}\\ \lambda\end{bmatrix}. \tag{27}$$

Using the last known solution $\mathbf{x}_0$ along the curve (starting point), the next prediction $\mathbf{x}_1^{(0)}$ is given as

$$\mathbf{x}_1^{(0)}=\mathbf{x}_0+s_0\mathbf{e}_0,\qquad |\mathbf{e}_0|=1, \tag{28}$$

where the upper index 0 indicates the initial guess used for Newton's method. The corresponding iteration scheme is generally formulated as

$$\mathbf{x}_1^{(i+1)}=\mathbf{x}_1^{(i)}-\big(\mathbf{J}(\mathbf{x}_1^{(i)})\big)^{-1}\mathbf{H}(\mathbf{x}_1^{(i)}), \tag{29}$$

where the Jacobian $\mathbf{J}$ is shortly written as

$$\mathbf{J}(\mathbf{x}_1^{(i)})\coloneqq\mathbf{H}'_{\mathbf{x}}(\mathbf{x}_1^{(i)})=\left.\frac{\partial\mathbf{H}(\mathbf{x})}{\partial\mathbf{x}}\right|_{\mathbf{x}=\mathbf{x}_1^{(i)}}. \tag{30}$$

The Jacobian associated with the continuation of the periodic orbit in one parameter is given as

$$\mathbf{J}(\mathbf{x})=\begin{bmatrix}\mathbf{G}'_{\mathbf{u}}(\mathbf{u},\lambda) & \mathbf{G}'_{\lambda}(\mathbf{u},\lambda)\\ \mathbf{e}_{0,\mathbf{u}}^{\top} & e_{0,\lambda}\end{bmatrix}. \tag{31}$$

In the formula above, the partial derivatives based on (23) can be expressed as

$$\mathbf{G}'_{\mathbf{u}}(\mathbf{u},\lambda)=\mathbf{D}-\mathbf{B}(\mathbf{u}) \tag{32}$$

and

$$\mathbf{G}'_{n}(\mathbf{u},n)=\frac{\partial\mathbf{D}(\Delta t)}{\partial\Delta t}\frac{\partial\Delta t}{\partial n},\quad \text{or} \tag{33}$$
$$\mathbf{G}'_{a}(\mathbf{u},a)=\frac{\partial\mathbf{Q}(\mathbf{u},a)}{\partial a}, \tag{34}$$

depending on the bifurcation parameter to be followed. On the one hand, in (33) the dependence on the spindle speed appears only in the spindle period $T=60/n$, and it is possible to express explicitly the derivatives using the chain rule ($\Delta t=T/N$, etc). On the other hand, in (34) the expression of the forces $\mathbf{F}$ include only the dependence on a, and hence the derivatives can again be constructed in a long, but straightforward manner.

Note that the technical implementation of the method requires adaptive step size and error checking in order to make sure that none of solutions are lost especially close to the turning points. One of the major numerical issue is the normalization of the parameters, since $n\sim10^3$, $a\sim10^{-3}$, $\mathbf{u}\sim10^{-6}$ are in different magnitudes (and units) and the continuation can easily break down if the step size is not small enough. This issue can be handled by introducing proper scaling factors w_i (e.g., $\mathbf{u}=w_1\tilde{\mathbf{u}}$ and $\lambda=w_2\tilde{\lambda}$) for the variables with different scales, and use the normalized variables $(\tilde{\mathbf{u}},\tilde{\lambda})$ for continuation instead. The norm of the new tangent $\mathbf{e}_0$ is therefore not dominated by one of the parameters; the numerical solver can use adaptive step size and turn around smooth fold points easily. The initial step size can be set to $s_0=10^{-4}$ and increase it if the solver converges quickly (e.g., $s_0\to1.2s_0$ until a maximum step size is reached) and reduce it if the local iterations fail to converge within a given number of iteration steps (e.g., $s_0\to0.5s_0$ and repeat the step). More technical issues and some recommended strategies can be found in [37].

B Stability of the periodic solutions

Since an equidistant spacing is used for the discretization, it is beneficial to combine the results with a corresponding method, such as the semi-discretization [9], since the required matrices are already computed during the iteration. For this purpose, the linearized equation (17) is reformulated. Let us introduce a small perturbation $\mathbf{v}(t)$ around the periodic motion $\overline{\mathbf{q}}(t)$ in the form

$$\mathbf{q}(t)=\overline{\mathbf{q}}(t)+\mathbf{v}(t). \tag{35}$$

After substituting (35) into (17), one can separate the equations as

$$\ddot{\overline{\mathbf{q}}}(t)+\hat{\mathbf{C}}\dot{\overline{\mathbf{q}}}(t)+\hat{\mathbf{K}}\overline{\mathbf{q}}(t)=\mathbf{U}^{\top}\mathbf{F}\big(t,\mathbf{U}\overline{\mathbf{q}}_t\big), \tag{36}$$

and

$$\ddot{\mathbf{v}}(t)+\hat{\mathbf{C}}\dot{\mathbf{v}}(t)+\hat{\mathbf{K}}\mathbf{v}(t)=\sum_{l=0}^{N_\tau}\mathbf{B}_l(t)\mathbf{v}(t-\tau_l), \tag{37}$$

where (36) includes the forced vibration, while (37) is the linearized equation around the periodic solution. Let us define the state corresponding to the variational equations as $\mathbf{w}(t)\coloneqq\mathrm{col}(\mathbf{v}(t),\dot{\mathbf{v}}(t))$. The solution of the TPDDE is given in the operator form as

$$\mathbf{w}_{t+T}=\boldsymbol{\mathcal{M}}(t,t+T)\mathbf{w}_t, \tag{38}$$

where $\boldsymbol{\mathcal{M}}(t,t+T)$ is the monodromy operator of the infinite-dimensional problem. The periodic solution is stable if all characteristic multipliers μ (eigenvalues) of the monodromy operator have modulus less than one. Since the monodromy operator is also infinite-dimensional, the stability of the system is analyzed by the discretized version of it, called monodromy matrix $\boldsymbol{\Phi}$ or (state) transition matrix. The transition matrix constructed by the semi-discretization method maps the discretized state vector $\mathbf{W}_0\coloneqq\mathrm{col}_{k=0}^{N}\mathbf{w}(-k\Delta t)$ to one period later, that is, $\mathbf{W}_N=\boldsymbol{\Phi}\mathbf{W}_0$, where N is the resolution of the discretization and $\Delta t=T/N$. Finally, the monodromy matrix is computed as

$$\boldsymbol{\Phi}=\mathbf{S}_{N-1}\mathbf{S}_{N-2}\cdots\mathbf{S}_0, \tag{39}$$

where $\mathbf{S}_k$s are the step matrices of the approximated discrete system for one numerical step. The multipliers μ are the eigenvalues of $\boldsymbol{\Phi}$. The details of the numerical method and the construction of the step matrices $\mathbf{S}_k$ are presented in the book of Insperger and Stepan [9].

References

1. F.W. Taylor. *On the Art of Cutting Metals*. Transactions of the ASME. American society of mechanical engineers, 1907.
2. J. Tlusty and L. Spacek. *Self-excited vibrations on machine tools*. Nakl. CSAV, Prague. in Czech., 1954.
3. S. Tobias and W. Fishwick. Theory of regenerative machine tool chatter. *The Engineer*, 205(7):199–204, 1958.
4. Jack K. Hale. *Theory of Functional Differential Equations*. Springer, 1977.
5. Yusuf Altintas. *Manufacturing Automation: Metal Cutting Mechanics, Machine Tool Vibrations, and CNC Design*. Cambridge University Press, 2 edition, 2012.

6. Y. Altintas and E. Budak. Analytical prediction of stability lobes in milling. *CIRP Annals*, 44(1):357 – 362, 1995.
7. S. D. Merdol and Y. Altintas. Multi frequency solution of chatter stability for low immersion milling. *Journal of Manufacturing Science and Engineering*, 126(3):459–466, August 2004.
8. K. Engelborghs, T. Luzyanina, K. J. in 't Hout, and D. Roose. Collocation methods for the computation of periodic solutions of delay differential equations. *SIAM Journal on Scientific Computing*, 22(5):1593–1609, jan 2001.
9. T. Insperger and G. Stepan. *Semi-Discretization for Time-Delay Systems: Stability and Engineering Applications*. Applied Mathematical Sciences. Springer New York, 2011.
10. Firas A. Khasawneh and Brian P. Mann. A spectral element approach for the stability of delay systems. *International Journal for Numerical Methods in Engineering*, 87(6):566–592, 2011.
11. Tamas Insperger, David Lehotzky, and Gabor Stepan. Regenerative delay, parametric forcing and machine tool chatter: A review. *IFAC-PapersOnLine*, 48(12):322–327, 2015.
12. David Hajdu, Tamas Insperger, Daniel Bachrathy, and Gabor Stepan. Prediction of robust stability boundaries for milling operations with extended multi-frequency solution and structured singular values. *Journal of Manufacturing Processes*, 30:281 – 289, 2017.
13. David Hajdu, Francesco Borgioli, Wim Michiels, Tamas Insperger, and Gabor Stepan. Robust stability of milling operations based on pseudospectral approach. *International Journal of Machine Tools and Manufacture*, 149:103516, 2020.
14. G. Totis and M. Sortino. Polynomial chaos-kriging approaches for an efficient probabilistic chatter prediction in milling. *International Journal of Machine Tools and Manufacture*, 157:103610, oct 2020.
15. Tony Schmitz, Aaron Cornelius, Jaydeep Karandikar, Christopher Tyler, and Scott Smith. Receptance coupling substructure analysis and chatter frequency-informed machine learning for milling stability. *CIRP Annals*, 71(1):321–324, 2022.
16. Tony Schmitz. A geometric approach to milling stability uncertainty. *Journal of Manufacturing Processes*, 105:307–312, November 2023.
17. M. E. Martellotti. An analysis of the milling process. *Trans. Am. Soc. mech. Engrs.*, 63(8):677–700, 1941.
18. W.A. Kline and R.E. DeVor. The effect of runout on cutting geometry and forces in end milling. *International Journal of Machine Tool Design and Research*, 23(2-3):123–140, jan 1983.
19. J.-J. Junz Wang and S. Y. Liang. Chip load kinematics in milling with radial cutter runout. *Journal of Engineering for Industry*, 118(1):111–116, feb 1996.
20. M. E. Martellotti. An analysis of the milling process, part II - down milling. *Journal of Fluids Engineering*, 67(4):233–251, may 1945.
21. Zhou-Long Li, Jin-Bo Niu, Xin-Zhi Wang, and Li-Min Zhu. Mechanistic modeling of five-axis machining with a general end mill considering cutter runout. *International Journal of Machine Tools and Manufacture*, 96:67–79, September 2015.
22. Xing Zhang, Jun Zhang, Bo Pang, DiaoDiao Wu, XiaoWei Zheng, and WanHua Zhao. An efficient approach for milling dynamics modeling and analysis with varying time delay and cutter runout effect. *The International Journal of Advanced Manufacturing Technology*, 87(9-12):3373–3388, apr 2016.
23. Jinbo Niu, Ye Ding, LiMin Zhu, and Han Ding. Mechanics and multi-regenerative stability of variable pitch and variable helix milling tools considering runout. *International Journal of Machine Tools and Manufacture*, 123:129–145, dec 2017.
24. Shanglei Jiang, Danian Zhan, Yang Liu, Yuwen Sun, and Jinting Xu. Modeling of variable-pitch/helix milling system considering axially varying dynamics with cutter runout offset and tilt effects. *Mechanical Systems and Signal Processing*, 168:108674, April 2022.
25. Shikang Li, Danian Zhan, Shuoxue Sun, and Yuwen Sun. Dynamics modeling and simultaneous identification of force coefficients for variable pitch bull-nose cutter milling considering process damping and cutter runout. *The International Journal of Advanced Manufacturing Technology*, 130(5–6):2877–2898, December 2023.
26. Yuebang Dai, Hongkun Li, Haibo Liu, Jianhua Yong, Chao Yang, Chaodong Wang, and Shengxian Liu. Dynamics and stability analysis of five-axis ball end milling with low radial immersion considering cutter runout. *Journal of Manufacturing Processes*, 92:479–499, April 2023.
27. Jinbo Niu, Ye Ding, Zunmin Geng, LiMin Zhu, and Han Ding. Patterns of regenerative milling chatter under joint influences of cutting parameters, tool geometries, and runout. *Journal of Manufacturing Science and Engineering*, 140(12), sep 2018.
28. R. P. Faassen; N. van de Wouw; H. Nijmeijer ; J. A. Oosterling. An improved tool path model including periodic delay for chatter prediction in milling. *Journal of Computational and Nonlinear Dynamics*, 2(2):167 – 179, 2007.
29. R.P.H. Faassen. *Chatter prediction and control for high-speed milling : modelling and experiments*. Phd thesis 1 (research tu/e / graduation tu/e), Mechanical Engineering, 2007.
30. Dániel Bachrathy, Gábor Stépán, and János Turi. State dependent regenerative effect in milling processes. *Journal of Computational and Nonlinear Dynamics*, 6(4), 2011.
31. G. Totis, Tamás Insperger, M. Sortino, and Gábor Stépán. Symmetry breaking in milling dynamics. *International Journal of Machine Tools and Manufacture*, 139:37–59, apr 2019.
32. David Hajdu, Oier Franco, Markel Sanz-Calle, Giovanni Totis, Jokin Munoa, Gabor Stepan, and Zoltan Dombovari. Stable tongues induced by milling tool runout. *International Journal of Machine Tools and Manufacture*, 206:104258, 2025.
33. Zoltan Dombovari, Yusuf Altintas, and Gabor Stepan. The effect of serration on mechanics and stability of milling cutters. *International Journal of Machine Tools and Manufacture*, 50(6):511 – 520, 2010.
34. Miklos Farkas. *Periodic Motions*. Springer-Verlag GmbH, 1994.
35. Jack K. Hale and Sjoerd M. Verduyn Lunel. *Introduction to Functional Differential Equations*. Springer New York, 1993.
36. Dirk Roose and Robert Szalai. *Continuation and Bifurcation Analysis of Delay Differential Equations*, pages 359–399. Springer Netherlands, 2007.
37. Yuri A. Kuznetsov. *Elements of Applied Bifurcation Theory*. Springer eBook Collection. Springer, New York, NY, 1995.

38. Willy J. F. Govaerts. *Numerical Methods for Bifurcations of Dynamical Equilibria*. Society for Industrial and Applied Mathematics, January 2000.
39. Pankaj Wahi and Anindya Chatterjee. Self-interrupted regenerative metal cutting in turning. *International Journal of Non-Linear Mechanics*, 43(2):111–123, March 2008.
40. Z. Dombovari, I. Laka, A. Bartfai, A. Karaca, E. Budak, G. Stepan, and J. Munoa. Directional factor as the key factor for chatter free robotic milling of light alloys. *CIRP Annals*, June 2025.
41. H.B. Keller. Numerical solution of bifurcation and nonlinear eigenvalue problems. In P. Rabinowitz, editor, *Applications of Bifurcation Theory*, pages 359–384, New York, 1977.
42. William J. Endres and Ming Loo. Modeling cutting process nonlinearity for stability analysis - Application to tooling selection for valve-seat machining. *Proc. 5th CIRP Workshop, West Lafayette, USA*, 2002.
43. Zsolt Iklodi and Zoltan Dombovari. Bifurcation analysis of piecewise-smooth engineering systems with delays through numeric continuation of periodic orbits. *Nonlinear Dynamics*, 112(24):21789–21818, August 2024.
44. Dániel Bachrathy and Gabor Stépán. Bisection method in higher dimensions and the efficiency number. *Periodica Polytechnica Mechanical Engineering*, 56(2):81–86, 2012.
45. Andrew Honeycutt and Tony Schmitz. A numerical and experimental investigation of period-n bifurcations in milling. *Journal of Manufacturing Science and Engineering*, 139(1), aug 2016.
46. Tony L. Schmitz, Jeremiah Couey, Eric Marsh, Nathan Mauntler, and Duke Hughes. Runout effects in milling: Surface finish, surface location error, and stability. *International Journal of Machine Tools and Manufacture*, 47(5):841–851, April 2007.
47. Yao Yan, Shu Zhang, Qing Guo, Jian Xu, and Kyung Chun Kim. Energy determines multiple stability in time-delayed systems. *Nonlinear Dynamics*, 102(4):2399–2416, November 2020.
48. Zoltan Dombovari, Alex Iglesias, Tamas G. Molnar, Giuseppe Habib, Jokin Munoa, Rachel Kuske, and Gabor Stepan. Experimental observations on unsafe zones in milling processes. *Philosophical Transactions of the Royal Society A: Mathematical, Physical and Engineering Sciences*, 377(2153):20180125, jul 2019.
49. Henrik T Sykora, David Hajdu, Zoltan Dombovari, and Daniel Bachrathy. Chatter formation during milling due to stochastic noise-induced resonance. *Mechanical Systems and Signal Processing*, 161:107987, dec 2021.
50. S. Léger, P. Larocque, and D. LeBlanc. Improved moore-penrose continuation algorithm for the computation of problems with critical points. *Computers & Structures*, 281:107009, June 2023.
51. Youheng Dong, Zhixin Wang, Xiaochen Mao, and Marco Amabili. On the combined iteration scheme of harmonic balance-pseudo arclength-extrapolation method applied to the nonlinear systems with nonlinear damping and time delay. *Nonlinear Dynamics*, May 2025.
52. W. Govaerts, Yu. A. Kuznetsov, H.G.E. Meijer, B. Al-Hdaibat, V. De Witte, A. Dhooge, W.Mestrom, A.M. Riet N. Neirynck, and B. Sautois. *MATCONT: Continuation toolbox for ODEs inMatlab*, 2019.
53. Robert Szalai. PDDE-CONT: A continuation and bifurcation software for delay-differential equations. Technical report, Budapest University of Technology and Economics, 2005.
54. J. Sieber, K. Engelborghs, T. Luzyanina, G. Samaey, and D. Roose. DDE-BIFTOOL v. 3.1.1 manual – bifurcation analysis of delay differential equations, 2017.